/16[illegible]

p-26

NASA Contractor Report 191015

Numerical Simulation of Free Shear Flows-Towards a Predictive Computational Aeroacoustics Capability

W.Y. Soh
Sverdrup Technology, Inc.
Lewis Research Center Group
Brook Park, Ohio

April 1993

Prepared for
Lewis Research Center
Under Contract NAS3–25266

(NASA-CR-191015) NUMERICAL SIMULATION OF FREE SHEAR FLOWS: TOWARDS A PREDICTIVE COMPUTATIONAL AEROACOUSTICS CAPABILITY (Sverdrup Technology) 26 p

N93-27097

Unclas

G3/02 0167902

National Aeronautics and
Space Administration

NUMERICAL SIMULATION OF FREE SHEAR FLOWS—
Towards a Predictive Computational Aeroacoustics Capability

W.Y. Soh
Sverdrup Technology, Inc.
Lewis Research Center Group
Brook Park, Ohio 44142

Summary

Implicit and explicit spatial differencing techniques with fourth order accuracy have been developed. The implicit technique is based on the Pade compact scheme. A Dispersion Relation Preserving concept has been incorporated into both of the numerical schemes. Two dimensional Euler computation of a spatially-developing free shear flow, with and without external excitation, has been performed to demonstrate the capability of numerical schemes developed. Results are in good agreement with theory and experimental observation regarding the growth rate of fluctuating velocity, the convective velocity, and the vortex-pairing process.

Introduction

Jet noise has emerged as a major issue in the High Speed Civil Transport Program. Noise reduction to an acceptable level set by FAR 36 Stage III is a challenging task to achieve. In order to accomplish this task, it has become increasingly important to be able to predict the sound pressure as a measure of noise level in the aeroacoustic research area. Far field noise is generated as a byproduct of the jet flow behind the exhaust nozzle. Therefore, understanding of this sound source is crucial. Lighthill [1], through his pioneering acoustic analogy, identified the sound source to be a fluctuating Reynolds stress. Numerous other works, both experimental and analytical, have been focused on the flow turbulence associated with the sound at a distance.

Experimental observations show that the sound power emitted from the jet column is greatest within 4 or 5 diameters downstream, and then decays rapidly through a transition region. This indicates that the initial development of the jet, before it becomes fully turbulent, should be clearly understood so that an accurate noise prediction can be made. The fully turbulent flow assumption yields analytic results which are far from reality in the developing regions. Freymuth [2] observed organized large eddy structures in a separated flow of a jet. Brown and Roshko [3] also found large vortical structure in a free shear layer. The identity of this large vortical structure is discernable even in the fully turbulent region far downstream. Winant and Browand [4] reported that a mechanism of the mixing layer growth is an interaction of adjacent large vortices. These investigators have shown that the flow in free shear layers such as jet and plane mixing flow is well hehaved and more organized than previously thought. Shear flow is dominated by large vortical structures, which are very predictable and controllable. These flows, which have been thought to be fully turbulent and therefore random and chaotic, have become research subjects with a quite different perspective since the observation of these organized structures. The separation of the organized flow entities from the fully random quantities make it possible to study turbulent shear flows in a certain deterministic way.

A turbulent flow field is made up of a range of length scales from the Kolmogorov scale to the integral scale. If numerical mesh size can be made fine enough to resolve the smallest scales which dissipate the kinetic energy, then direct numerical simulation (DNS) is the tool to obtain the entire turbulent flow structure. However, the dissipative scale becomes finer as the Reynolds number is increased and the practical hardware limitation is rapidly reached. Therefore, the DNS method is limited to simulating only low Reynolds number turbulence. For practical computation of higher Reynolds number flows, small scale fluctuations can be modeled so that desired large scale eddies can be computed directly, while proper dissipation is provided by the small scale eddy model. This approach, which is referred to as large eddy simulation (LES), has been successfully employed in many flows with practical applications.

In order to obtain the flow field as the source of sound using DNS or LES the simulations must be performed using numerical techniques with least distortion and diffusive characteristics. The source of numerical diffusion and phase error is known to be mainly from the numerical formulation of convective terms. This numerical artifact gets worse for high Reynolds number flow simulations. Typically, free shear flows of interest have very high Reynolds numbers. Therefore, a higher order accurate numerical scheme which meets the previously mentioned requirements is needed. To develop a highly accurate numerical scheme for this purpose, it will be appropriate to consider only an inviscid flow. Fourth order explicit and implicit differencing schemes with a Dispersion Relation Preserving property are introduced in the context of the numerical formulation of the Euler equations. A Pade compact scheme is used in the implicit differencing formulation. A plane shear flow generated by two streams of air with different velocities is chosen as an example to validate numerical schemes. Subsonic and supersonic results will be shown and discussed here together with physical observations of the spatial growth of fluctuating velocity, the development of large vortical structure, and the vortex-pairing process.

Governing Equation

The variables $T, \rho, \mathbf{x}, \mathbf{u}, t, p$, and e represent dimensionless quantities of temperature, density, position, velocity, time, pressure, and total energy per mass. The nondimensionalization is based on reference quantities of $T_r^*, \rho_r^*, l_r^*, u_r^*, p_r^*$, and e_r^*. Additional definitions are $t_r^* = l_r^*/u_r^*$, $p_r^* = \rho_r^* {u_r^*}^2$, and $e_r^* = {u_r^*}^2$. Then, the non-dimensional equation of state can be written as follows :

$$p = \frac{\rho T}{\gamma M_r^2} \quad \text{with} \quad T = \gamma(\gamma - 1)M_r^2\left(e - \frac{u^2 + v^2}{2}\right)$$

where γ is the ratio of specific heats, $M_r = u_r^*/\sqrt{\gamma R^* T_r^*}$, and R^* is the gas constant. The Euler equations in two-dimensional Cartesian coordinates $(x,\, y)$ are :

$$\frac{\partial \mathbf{q}}{\partial t} + \frac{\partial \mathbf{f}}{\partial x} + \frac{\partial \mathbf{g}}{\partial y} = \mathbf{s} \quad \text{where} \quad \mathbf{q} = (\rho, \rho u, \rho v, \rho e)^T \tag{1}$$

$$\mathbf{f} = \begin{pmatrix} \rho u \\ \rho u^2 + p \\ \rho uv \\ (\rho e + p)u \end{pmatrix} \quad \text{and} \quad \mathbf{g} = \begin{pmatrix} \rho v \\ \rho uv \\ \rho v^2 + p \\ (\rho e + p)v \end{pmatrix}$$

$\mathbf{s}$ is the source term. The dimensionless speed of sound, c, becomes $\sqrt{T}/M_r$. Equation (1) can be written in a generalized coordinates (ξ, η) as :

$$\frac{\partial \mathbf{Q}}{\partial t} + \frac{\partial \mathbf{F}}{\partial \xi} + \frac{\partial \mathbf{G}}{\partial \eta} = \mathbf{S} \quad \text{where} \quad \mathbf{Q} = J\mathbf{q}, \quad \mathbf{S} = J\mathbf{s} \tag{2}$$

$$J = x_\xi y_\eta - y_\xi x_\eta = (\xi_x \eta_y - \xi_y \eta_x)^{-1}, \quad \mathbf{F} = J(\xi_x \mathbf{f} + \xi_y \mathbf{g}), \quad \mathbf{G} = J(\eta_x \mathbf{f} + \eta_y \mathbf{g})$$

Formulation of Difference Scheme

Basically, two different formulations are presented for a spatial differencing, one is the explicit and the other is implicit differencing technique. A Pade compact differencing formulation is used for the implicit method developed. Pade compact scheme [5,6] has also been previously used in flow computations. All of the methods presented are fourth order accurate in space and incorporated with the Dispersion Relation Preserving concept proposed by Tam and Webb [7].

Explicit Differencing

The fourth order finite-difference formulation of $\frac{\partial f}{\partial x}$, which is denoted by f', is given by :

$$f'(x) = \frac{4}{3}\left(\frac{f_{i+1} - f_{i-1}}{2h}\right) - \frac{1}{3}\left(\frac{f_{i+2} - f_{i-2}}{4h}\right)$$

where the subscript i is the mesh index, h the uniform mesh size. The above expression is solely based on the trunction of Taylor series. In unsteady flow computation, the order of accuracy is not the only issue to obtain a reliable solution. Unsteady flows by nature contain wave trains, which must be well resolved. Numerical difference formulations, constructed solely by truncation of Taylor series, do not guarantee wave preservation even when higher order differences are used. The wave becomes severely distorted as the wave number, or the frequency in a time space, is increased and eventually a physical interpretation of the results becomes impossible. Tam and Webb [7] proposed a difference scheme, which is called the Dispersion Relation Preserving (hereinafter it will be called DRP) scheme, in which the dispersion characteristics follows closely to that of original differential form. For example, suppose we need a fourth order explicit difference scheme using six neighboring points, then the finite difference formulation of $f'(x)$ becomes :

$$f'(x) = a\,\frac{f_{i+1} - f_{i-1}}{2h} + b\,\frac{f_{i+2} - f_{i-2}}{4h} + c\,\frac{f_{i+3} - f_{i-3}}{6h} \tag{3}$$

To be fourth order accurate, the constants b and c are $\frac{9-8a}{5}$ and $\frac{3a-4}{5}$. For $c = 0$ the above expression uses four adjacent points, which is solely based on the truncation of Taylor series. Equation (3) contains one free parameter, say a, which will be optimized. To introduce the DRP scheme, we define the Fourier transform of $f(x)$ and its inverse as :

$$\tilde{f}(w) = \frac{1}{\sqrt{2\pi}} \int_{-\infty}^{+\infty} f(x) e^{-iwx}\, dx$$

$$f(x) = \frac{1}{\sqrt{2\pi}} \int_{-\infty}^{+\infty} \tilde{f}(w) e^{iwx}\, dw$$

Fourier transforming equation (3) by the above definition gives :

$$i\kappa \tilde{f}(w) = i(a \sin \kappa + \frac{b}{2} \sin 2\kappa + \frac{c}{3} \sin 3\kappa)\tilde{f}(w)$$

where κ is defined to be wh. Notice that with the difference approximation given by (3), an input wave number of κ is distorted into a different wave number of $\tilde{\kappa}$ which is defined to be $a \sin \kappa + \frac{b}{2} \sin 2\kappa + \frac{c}{3} \sin 3\kappa$. It is needed to optimize the free parameter a so that the responding wave $\tilde{\kappa}$ depicts the input wave κ closely over the wave number space of interest. In reference [7] the function to be minimized is chosen as :

$$I = \int_{-\pi/2}^{\pi/2} (\kappa - \tilde{\kappa})^2\, d\kappa \tag{4}$$

The limits of integral $-\frac{\pi}{2}$ and $\frac{\pi}{2}$ is selected under an assumption that a minimum of four mesh intervals are required to resolve a wave. This appears quite plausible because the value of I becomes very small over a wide range of a for longer waves, say $8h, 16h$ waves. For these longer waves optimization based on DRP concept becomes less meaningful.

Figure 1 shows the numerical behavior of $\tilde{\kappa}$ against κ for different values of a. The straight line represents the exact differentiation. It is seen that the curve for $a = 1.59853$, which has been evaluated to be optimum value by reference [7], closely follows the straight line for κ up to about 0.5, while the sixth order counterpart is valid up to about κ of 0.4. A conventional fourth order differencing, which is obtained at $a = \frac{4}{3}$, restricts its validity only to a long wave range, say $\kappa < 0.3$. There is no doubt that the second order accurate scheme is severely limited to resolving only long waves.

Pade Compact Differencing Scheme

The Pade compact difference scheme used here is an implicit method in space. This scheme uses a symmetric numerical stencil in a compact form so that only a tridiagonal or penta-diagonal matrix inversion is needed. Even for higher order formulations the compactness is still maintained. Following general form of the Pade difference scheme can be used to obtain a difference form of f'.

$$\ldots + \alpha_2 f'_{i-2} + \alpha_1 f'_{i-1} + f'_i + \alpha_1 f'_{i+1} + \alpha_2 f'_{i+2} + \ldots = \ldots + a_2 \frac{f_{i+2} - f_{i-2}}{4h} + a_1 \frac{f_{i+1} - f_{i-1}}{2h}$$

In the present formulation we use the following form to assure that only the tridiagonal matrix inversion is required to obtain a solution for $f'(x)$.

$$\alpha f'_{i-1} + f'_i + \alpha f'_{i+1} = b\,\frac{f_{i+2} - f_{i-2}}{4h} + a\,\frac{f_{i+1} - f_{i-1}}{2h} \tag{5}$$

With $a = \frac{2\alpha+4}{3}$ and $b = \frac{4\alpha-1}{3}$, this formulation is forth order accurate, and α ia a free parameter. Equation (5) can be reduced to sixth order accuracy if α is set to $\frac{1}{3}$. It is straightforward to make the Pade formulation (5) DRP based since it has a built-in free parameter α to be optimized. Using the same definition of Fourier transform as used in the explicit differencing case, we can formulate the wave number relation as :

$$\tilde{\kappa} = \frac{a \sin\kappa + \frac{b}{2}\sin 2\kappa}{1 + 2\alpha\cos\kappa}$$

The optimum value of α is computed to be 0.35619 when the integral I, defined in (4), is minimized. Figure 2 illustrates the wave number relation between κ the input wave and $\tilde{\kappa}$ the response wave. As was the case with the explicit difference scheme, better wave behavior is observed for the fourth order scheme with the optimum α than for the sixth order differencing with $\alpha = \frac{1}{3}$. The curve for $\alpha = \frac{1}{4}$ is of the most compact fourth order scheme. Figure 3 is the comparison made among the six cases. The most compact fourth order scheme has broader range of wave number than the optimum case of the explicit scheme. However, for a computation which employs a large number of mesh points such as in a three dimensional flow simulation, the optimized explicit scheme can be a good alternative to the implicit differencing if only a moderate number of mesh points are added more for the resolution of all waves under consideration.

Comments on Finite Volume Scheme

Finite volume formulations have been favorably used in the CFD community because it mimics an integral form of physical equation on a computation cell. The surface values, known as fluxes, are of primary concern. The finite volume formulation of the flow equation is conservative since the fluxes are cancelled out when a global summation is carried out over all the computation cells. For example, the one dimensional equation, $\frac{\partial u}{\partial t} + \frac{\partial F}{\partial x} = 0$, can be integrated over a space interval of h to give :

$$\frac{\partial}{\partial t}\int_{-\frac{h}{2}}^{+\frac{h}{2}} u\,dx + F_{i+\frac{1}{2}} - F_{i-\frac{1}{2}} = 0$$

where F is a function of u, h uniform mesh size, and the subscripts $i - \frac{1}{2}$ and $i + \frac{1}{2}$ denote the left and right cell boundaries. A second order spatial accuracy can be achieved by representing the integral, $\int u\,dx$, by $u_i h$ and the fluxes $F_{i+\frac{1}{2}}$ and $F_{i-\frac{1}{2}}$ to be $\frac{1}{2}(F_{i+1} + F_i)$ and $\frac{1}{2}(F_{i-1} + F_i)$. This leads to the symmetric finite difference formulation of :

$$\frac{\partial u}{\partial t} + \frac{\partial F}{\partial x} = \frac{\partial u_i}{\partial t} + \frac{F_{i+1} - F_{i-1}}{2h} + O(h^2)$$

For higher order spatial accuracy, the finite volume formulation is proposed as the following :

$$\int_{-\frac{h}{2}}^{+\frac{h}{2}} (\frac{\partial u_i}{\partial t} + \frac{\partial F}{\partial x}) \, dx = h \sum_{k=-N}^{+N} a_k \frac{\partial}{\partial t}(u_{i+k}) + F_{i+\frac{1}{2}} - F_{i-\frac{1}{2}}$$

Expanding $F_{i-\frac{1}{2}}$ and $F_{i+\frac{1}{2}}$ about the point x_i in the Taylor series and then using $F''' = -\partial u''/\partial t$, $F''''' = -\partial u''''/\partial t$ (prime denotes a derivative with respect to the spatial variable x) relationships, we can obtain the following for fourth order accuracy.

$$\frac{\partial u}{\partial t} + \frac{\partial F}{\partial x} = \frac{\partial}{\partial t}(\frac{1}{24}u_{i-1} + \frac{22}{24}u_i + \frac{1}{24}u_{i+1}) + \frac{F_{i+\frac{1}{2}} - F_{i-\frac{1}{2}}}{h} + O(h^4) \qquad (6)$$

The quantity in the parenthesis of the time term is a cell average value of u and the fluxes are evaluated in a symmetric manner as:

$$F_{i+\frac{1}{2}} = \frac{9\,(F_{i+1} + F_i) - (F_{i+2} + F_{i-1})}{16} \quad \text{and} \quad F_{i-\frac{1}{2}} = \frac{9\,(F_{i-1} + F_i) - (F_{i-2} + F_{i+1})}{16}$$

Equation (6) is a time implicit form which calls for a matrix inversion. A multi-dimensional extension of the finite volume formulation becomes increasingly complicated.

As a coding practice in the present work, a finite volume like formulation is used for the spatial discretization through a definition as :

$$f' = \frac{\tilde{f}_{i+\frac{1}{2}} - \tilde{f}_{i-\frac{1}{2}}}{h} \qquad (7)$$

The value $\tilde{f}$ can be treated as a cell interface value only by analogy, but it is not the physical value at the designed accuracy. (up to the second order accuracy, $\tilde{f}$ represents a physical quantity at the interface) For the explicit differencing, we propose the following :

$$\tilde{f}_{i-\frac{1}{2}} = A_1 \frac{f_i + f_{i-1}}{2} + A_2 \frac{f_{i+1} + f_{i-2}}{2} + A_3 \frac{f_{i+2} + f_{i-3}}{2}$$

Using the definition (7) for equation (3), we arrive at the following constants :

$$A_1 = a + \frac{b}{2} + \frac{c}{3}, \quad A_2 = \frac{b}{2} + \frac{c}{3}, \quad A_3 = \frac{c}{3}$$

For the Pade compact scheme, we also propose the following formulation, which is similar to equation (5), to obtain an interface value at the point $i - \frac{1}{2}$.

$$\alpha\tilde{f}_{i-\frac{3}{2}} + \tilde{f}_{i-\frac{1}{2}} + \alpha\tilde{f}_{i+\frac{1}{2}} = B_1 \frac{f_i + f_{i-1}}{2} + B_2 \frac{f_{i+1} + f_{i-2}}{2} \qquad (8)$$

Rewriting a similar equation centered at $i + \frac{1}{2}$ and then subtracting the original equation (8) from it gives :

$$\alpha(\tilde{f}_{i-\frac{1}{2}} - \tilde{f}_{i-\frac{3}{2}}) + \tilde{f}_{i+\frac{1}{2}} - \tilde{f}_{i-\frac{1}{2}} + \tilde{\alpha}(\tilde{f}_{i+\frac{3}{2}} - \tilde{f}_{i+\frac{1}{2}}) = B_2 \frac{f_{i+2} - f_{i-2}}{2} + (B_1 - B_2) \frac{f_{i+1} - f_{i-1}}{2}$$

By using the definition of equation (7), the above equation reduces to

$$\alpha f'_{i-1} + f'_i + \alpha f'_{i+1} = 2B_2\,\frac{f_{i+2} - f_{i-2}}{4h} + (B_1 - B_2)\,\frac{f_{i+1} - f_{i-1}}{2h} \tag{9}$$

By inspecting equation (9) against equation (5), the constants are found to be $B_1 = \frac{8\alpha+7}{6}$, and $B_2 = \frac{4\alpha-1}{6}$. For $\alpha = \frac{1}{4}$ only two neighboring two points are used, which has the most compact form in the right hand side of equation (9).

Using $\tilde{\mathbf{F}}$ and $\tilde{\mathbf{G}}$ defined in a similar method as the $\tilde{f}$, we can spatially discretize the Euler equation (2) by setting $\Delta\xi = \Delta\eta = 1$ as :

$$\frac{\partial \mathbf{Q}}{\partial t} + \tilde{\mathbf{F}}_{i+\frac{1}{2}j} - \tilde{\mathbf{F}}_{i-\frac{1}{2}j} + \tilde{\mathbf{G}}_{ij+\frac{1}{2}} - \tilde{\mathbf{F}}_{ij-\frac{1}{2}} = \mathbf{S}$$

The indices i and j are for the ξ and η directions, respectively.

Time Advancing Scheme

The four-stage Runge-Kutta technique [8] is adopted for the explicit formulation in time. To obtain new flow variables at $t = (n+1)\Delta t$ from known data at $t = n\Delta t$ equation (2) is used to advance the solution in time as follows :

$$\begin{aligned}
\mathbf{Q}^{(1)} - \mathbf{Q}^n &= \alpha_1\,\Delta t\mathbf{W}^{(0)} \\
\mathbf{Q}^{(2)} - \mathbf{Q}^n &= \alpha_2\,\Delta t\mathbf{W}^{(1)} \\
\mathbf{Q}^{(3)} - \mathbf{Q}^n &= \alpha_3\,\Delta t\mathbf{W}^{(2)} \\
\mathbf{Q}^{(4)} - \mathbf{Q}^n &= \alpha_4\,\Delta t\mathbf{W}^{(3)} + \mathbf{D}
\end{aligned}$$

where $\mathbf{W}^{(k)}$ denotes $\mathbf{S} - \partial\mathbf{F}/\partial\xi - \partial\mathbf{G}/\partial\eta$ evaluated at the k-th stage. The stage 0 and 4 are at the time, $n\Delta t$ and $(n+1)\Delta t$. The parameters, $\alpha_1, \alpha_2, \alpha_3, \alpha_4$, are given to be $\frac{1}{4}, \frac{1}{3}, \frac{1}{2}, 1$. This time difference is second order accurate and the intermediate variables are not stored at every stage.

A numerical dissipation term $\mathbf{D}$ is added during the fourth stage to enhance the numerical stability. The dissipation term is introduced to be of sixth order so that our fourth order accuracy remains intact.

$$\mathbf{D} = \omega_e\,J\left(\frac{\partial^6 \mathbf{q}}{\partial\xi^6} + \frac{\partial^6 \mathbf{q}}{\partial\eta^6}\right)$$

where ω_e is a constant and $\partial^6\mathbf{q}/\partial\xi^6$ is given by :

$$\frac{\partial^6 \mathbf{q}}{\partial\xi^6} = 15(\mathbf{q}_{i+1j} + \mathbf{q}_{i-1j}) - 6(\mathbf{q}_{i+2j} + \mathbf{q}_{i-2j}) + (\mathbf{q}_{i+3j} + \mathbf{q}_{i-3j}) - 20\mathbf{q}_{ij}$$

The derivative $\partial^6\mathbf{q}/\partial\eta^6$ in the η direction is obtained in the similar manner. This numerical dissipation is applied to all internal points.

Boundary Condition

The boundary treatment considered here is a combination of characteristic and algebraic boundary conditions. The characteristic boundary condition solves the governing equation in a characteristic form in each coodinate direction and the algebraic boundary condition is the given boundary conditions such as temperature, total temperature, velocity, *etc.* Equation (2) is written in a non-conservative form as:

$$\frac{\partial \mathbf{q}}{\partial t} + \mathbf{A}\,\frac{\partial \mathbf{q}}{\partial \xi} + \mathbf{B}\,\frac{\partial \mathbf{q}}{\partial \eta} = 0 \quad \text{where} \quad \mathbf{A} = \frac{\partial \mathbf{F}}{\partial \mathbf{q}} \quad \text{and} \quad \mathbf{B} = \frac{\partial \mathbf{G}}{\partial \mathbf{q}}$$

For the ξ direction, equation (2) with a transformation $d\mathbf{q} = \mathbf{R}_\xi d\tilde{\mathbf{q}}$ becomes

$$\frac{\partial \tilde{\mathbf{q}}}{\partial t} + \mathbf{R}_\xi^{-1}\mathbf{A}\mathbf{R}_\xi \frac{\partial \tilde{\mathbf{q}}}{\partial \xi} + \mathbf{R}_\xi^{-1}\mathbf{B}\mathbf{R}_\xi \frac{\partial \tilde{\mathbf{q}}}{\partial \eta} = 0$$

If we construct the matrix $\mathbf{R}_\xi$ such that the eigenvectors of the matrix $\mathbf{A}$ constitute its columns then the matrix by a similarity transform becomes a diagonal matrix, whose entries are the eigenvalues of $\mathbf{A}$ such that

$$\mathbf{R}_\xi^{-1}\mathbf{A}\mathbf{R}_\xi = \mathbf{\Lambda}_\xi = \mathrm{diag}(U, U, U + a_\xi, U - a_\xi)$$

where $a_\xi = c\sqrt{\xi_x^2 + \xi_y^2}$. Here, c is the speed of sound defined to be $\sqrt{T}/M_r$, and $U = \xi_x u + \xi_y v$. In the same way, for the η direction the diagonal matrix becomes :

$$\mathbf{R}_\eta^{-1}\mathbf{B}\mathbf{R}_\eta = \mathbf{\Lambda}_\eta = \mathrm{diag}(V, V, V + a_\eta, V - a_\eta)$$

where $a_\eta = c\sqrt{\eta_x^2 + \eta_y^2}$, and $V = \eta_x u + \eta_y v$. The characteristic equations are then rewritten in each coordinate direction to be:

$$\mathbf{R}_\xi^{-1}\frac{\partial \mathbf{q}}{\partial t} + \mathbf{\Lambda}_\xi \mathbf{R}_\xi^{-1}\frac{\partial \mathbf{q}}{\partial \xi} + \frac{\mathbf{R}_\xi^{-1}}{J}\frac{\partial \mathbf{G}}{\partial \eta} = 0 \quad \text{and} \quad \mathbf{R}_\eta^{-1}\frac{\partial \mathbf{q}}{\partial t} + \mathbf{\Lambda}_\eta \mathbf{R}_\eta^{-1}\frac{\partial \mathbf{q}}{\partial \eta} + \frac{\mathbf{R}_\xi^{-1}}{J}\frac{\partial \mathbf{F}}{\partial \xi} = 0$$

$$\mathbf{R}_\kappa = \begin{pmatrix} 1 & 0 & \frac{\rho}{\sqrt{2}\,c} & \frac{\rho}{\sqrt{2}\,c} \\ u & \rho\tilde{\kappa}_y & \frac{\rho}{\sqrt{2}}(\frac{u}{c} + \tilde{\kappa}_x) & \frac{\rho}{\sqrt{2}}(\frac{u}{c} - \tilde{\kappa}_x) \\ v & -\rho\tilde{\kappa}_x & \frac{\rho}{\sqrt{2}}(\frac{v}{c} + \tilde{\kappa}_y) & \frac{\rho}{\sqrt{2}}(\frac{v}{c} - \tilde{\kappa}_y) \\ \frac{\Phi}{\gamma-1} & \rho(u\tilde{\kappa}_y - v\tilde{\kappa}_x) & \Psi + \frac{\rho}{\sqrt{2}}\theta & \Psi - \frac{\rho}{\sqrt{2}}\theta \end{pmatrix}$$

where :

$$\mathbf{R}_\kappa^{-1} = \begin{pmatrix} 1 - \frac{\Phi}{c^2} & (\gamma-1)\frac{u}{c^2} & (\gamma-1)\frac{v}{c^2} & -\frac{\gamma-1}{c^2} \\ \frac{-\tilde{\kappa}_y u + \tilde{\kappa}_x v}{\rho} & \frac{\tilde{\kappa}_y}{\rho} & \frac{-\tilde{\kappa}_x}{\rho} & 0 \\ \frac{-\theta}{\sqrt{2}\rho} + \frac{\Phi}{\sqrt{2}\rho c} & \frac{\tilde{\kappa}_x}{\sqrt{2}\rho} + \frac{(1-\gamma)u}{\sqrt{2}\rho c} & \frac{\tilde{\kappa}_y}{\sqrt{2}\rho} + \frac{(1-\gamma)v}{\sqrt{2}\rho c} & \frac{\gamma-1}{\sqrt{2}\rho c} \\ \frac{\theta}{\sqrt{2}\rho} + \frac{\Phi}{\sqrt{2}\rho c} & \frac{-\tilde{\kappa}_x}{\sqrt{2}\rho} + \frac{(1-\gamma)u}{\sqrt{2}\rho c} & \frac{-\tilde{\kappa}_y}{\sqrt{2}\rho} + \frac{(1-\gamma)v}{\sqrt{2}\rho c} & \frac{\gamma-1}{\sqrt{2}\rho c} \end{pmatrix}$$

$$\text{and} \quad \tilde{\kappa}_x = \frac{\kappa_x}{\sqrt{\kappa_x^2 + \kappa_y^2}}, \quad \tilde{\kappa}_y = \frac{\kappa_y}{\sqrt{\kappa_x^2 + \kappa_y^2}}, \quad \kappa = \xi, \eta$$

$$\theta = \tilde{\kappa}_x u + \tilde{\kappa}_y v, \quad \Phi = \frac{\gamma - 1}{2}(u^2 + v^2), \quad \Psi = \frac{\rho\Phi}{\sqrt{2}(\gamma - 1)c} + \frac{\rho c}{\sqrt{2}(\gamma - 1)}$$

Hedstrom [9] proposed that the non-reflecting boundary condition can be constructed by setting any eigenvalue, which is the element of $\mathbf{\Lambda}$, to be zero, if a wave is incoming towards the computational domain. Thompson [10] further extends this method and Lele [5] used the same boundary condition in the simulation of a free shear flow.

Application

In the present study Euler computations of plane shear flow are presented to validate the numerical method developed. For this validation, computional results of spatially developing flow are examined against linear theories, experimental data, and flow visualizations. The initial shear is given as the axial velocity distribution at $x = 0$, where x is the downstream variable. Initial vorticity thickness of the shear $\delta\omega_0$, which is defined as $(u_f^* - u_s^*)/(du^*/dy^*)_{max}$, is chosen as the reference length l_r^*. Quantities with asterisks are dimensional, subscripts f and s denote faster and slower speeds, respectively. The maximum derivative is taken at the inflection point at $y = 0$. Then, the initial shear profile is given as :

$$u = \lambda_s \tanh(2y) + 1, \quad \lambda_s = \frac{\Delta u^*}{2u_r^*} \tag{10}$$

where $\Delta u^* = u_f^* - u_s^*$, $u_r^* = (u_f^* + u_s^*)/2$, and the reference velocity in this case is the average speed of two streams. The momentum thickness, θ, which is used as a reference length scale in both theoretical and experimental analysis, becomes $\delta\omega_0/4$ for the shear given by (10). All the flow computations is carried out by assuming that mixing of two streams occurs at an uniform temperature. The other flow parameters chosen are: $T_r^* = 298^{O}\mathrm{K}$, $l_r^* = 0.00254$ m, and $\rho_r^* = 1.1839\ \mathrm{Kg/m^3}$.

Figure 4 illustrates two grids used. Grid I (240×120) and Grid II (300×160) are stretched in both y and x directions. In Grid I mesh size Δx varies between 0.4 and 1.568 with $0.15 \leq \Delta y \leq 0.4$ at the inlet and $0.333 \leq \Delta y \leq 0.864$ at the exit plane. The inlet extends between $-12.43 \leq y \leq 12.43$ and the exit plane between $-32.7 \leq y \leq 32.7$, and x reaches 196.5. In Grid II mesh size Δx varies between 0.516 and 0.84. Inlet and exit have the same height of $-25.8 \leq y \leq +25.8$ with $\Delta y_{min} = 0.12$ and $\Delta y_{max} = 0.576$. The downstream extends to $x = 206$.

Subsonic flows are simulated with and without external excitation on the initial shear. Mach numbers of the two streams considered here are 0.6 and 0.3, in which u_r^*=155.768 m/s, $M_r = 0.45$, and p_r^* is 2.873 K Pa. At the inlet, u defined by (10), $v = 0$, $T = 1$ are given and one characteristic equation is solved for the outgoing acoustic wave. At the exit, the characteristic equations are solved for the three outgoing waves. For the other incoming acoustic wave, the characteristic equation is also imposed with its incoming wave velocity set to zero. On the side boundaries, all the characteristic equations are computed by setting the wave velocity to zero if the wave is incoming towards the computational domain. The flow case with no excitation, which is naturally acquired flow, is simulated first. A forcing is then given later on the v velocity at the inlet from the natural flow solution to excite the flow.

Figures 5-(a,b,c) show the contour plots of Mach number, vorticity, and the static pressure at an instant in time. A large vortical structure is clearly seen in the Mach number and the vorticity contour plots as shown by Figures 5-(a) and (b). The static pressure contour plot of Figure 5-(c) supports existence of this vortical structure by aligning its local mimima with the centers of the vortices depicted in the Mach number and the vorticity contour plots. This train of local pressure minima and maxima is the basis of analytic estimation of the convective velocity at which the large vortical structure travels. The vorticity contour plot is chosen hereafter as an appropriate visual device to examine the large flow structure. The vorticity contour plots in Figures 6 through 9 show a spatial evolution of shear flow with time. The convective velocity can be found from the time history of the vorticity contours. The simulation using the Pade differencing with $\alpha = 0.3$ and 0.35619 predicted the convective velocity, u_c, of 0.99. In the explicit computation u_c has a value between 0.96 and 1.02. From the four cases shown in Figures 6 through 9, it can be concluded that the convective velocity is about unity, which is the average velocity of the two streams. Brown and Roshko [3] found that the large eddies travel at a constant velocity, which is the average speed of the two streams, and this velocity is independent of size or location of the eddy. Papamoschou and Roshko [11] derived the same result. This convective velocity is identical with the computed value and the present results also confirm an earlier observation that the convective velocity is independent of eddy location and size. The only exception is that the convective velocity varies when two successive vortices merge into one, which is often referred to as a vortex pairing. In this pairing process, the vortex which travels behind picks up speed to catch up with another vortex proceeding ahead, then the two slide on each other and coalesce. After the completion of vortex pairing the convective velocity becomes constant again until another pairing occurs further downstream. This vortex pairing process is illustrated in the vorticity contour plots. Figure 10 shows the trajectories of vortices, which shows the birth, pairing, convecting, and further pairing of vortices. Parallel slopes on the $x - t$ diagram, which is the convective velocity, are clearly seen to be constant regardless of the vortex location.

An unforced shear flow exhibits a distributed spectrum in its fluctuating quantity. Figure 11 shows this for the u velocity spectra at $y = 0$ and various downstream locations. A peak in the spectrum is clearly seen in this unforced flow. The frequency for the peak in the spectrum is referred to as the most preferred frequency. The Strouhal number, St, is used as a dimensionless frequency and defined to be $f^*\theta/u_r^*$ with f^* the frequency in Hz, θ the initial momentum thickness. In the early flow development, the u spectrum has its peak at $St = 0.021$. This persists to some location downstream, then eventually, the lower frequency of $St = 0.0086$ becomes dominant far downstream. This agrees with the general observation that lower frequency wave, whose wave length is longer, survives further downstream than a higher frequency wave. Linear theories by Michalke [12], and Monkewitz and Huerre [13] show that the most amplified frequency is about $St = 0.033$. In jet flow, Freymuth [2] found the growth rate observed experimentally agrees very well with the theory for St up to about 0.024, and remains constant for $St \geq 0.024$. This value is very close to the computed St of 0.021. In light of those results, it appears that the most preferred frequency, which is acquired naturally, has a lower value than the most amplified frequency predicted by linear theory.

It is known from linear theory that a free shear flow is unstable under presence of a disturbance. The disturbance introduced grows exponentially either in space or in time. The initial shear layer undergoes wave propagation in the presence of a background disturbance, which is due to the truncation error caused by a discretization of the flow equations. Traveling instability waves get intensified to a certain level of magnitude. In Figures 6-9, the shear layer appears wavy, yet it is well connected up to x of 60 to 80 depending upon time. The shear layer, then, rolls up into a discrete vortex and convects downstream. In the early flow development stage before the vortex roll-up, there is a region where linear theory is valid. This linear region can be verified by checking for exponential growth in the magnitude of fluctuating u velocity. The root-meam-square of fluctuation of u, denoted by u'_{rms}, is used as a measure of the magnitude. Figures 12-(a),(b), and (c) show the region in which a logarithmic scale of u'_{rms} grows linearly for various y locations. Sharp increase near $x = 0$ should be neglected since the boundary condition imposed at the inlet influences the flow solution in this region. It appears that the slope varies also with y and the maximum slope is shown on the slower fluid side. A growth rate s is defined to be $d(\ln u'_{\text{rms}})/dx$. Then, values of s for the unforced shear flow shown in Figure 12-(a) are 0.096, 0.102, 0.106, 0.105, 0.1, 0.099, and 0.096 at y=-4, -3, -2, -1, -0.06, 1, 2, respectively. Figure 12-(b) presents curves for when forcing is applied at its most preferred upstream frequency at St of 0.021. Values of the slope are the same as those for unforced flow, because natural shear flow is already dominated by the wave of that frequency. However, the linear region near the inflection point becomes hardly discernable. This can be an indication that nonlinearity takes place earlier than the unforced case. With lower frequency forcing, s has smaller values of 0.087, 0.096, 0.098 at y=-3, -2, -1, respectively. It is difficult to find the constant value of s near the inflecton point and in the faster fluid territory. It can be interpreted that the two waves, one of forcing frequency and the other of upstream most preferred frequency, interact nonlinearly. However, it appears in common that u'_{rms} grows up to a certain magnitude, and then levels off. The u'_{rms} varies in a mildly oscillatory manner further downstream, which is not shown in the figure. In Figure 12-(a) and (c), u'_{rms} becomes magnified up to about 10 %, and 13 % in Figure 12-(b).

The u'_{rms} discussed above is not for a single frequency, but for all the frequency content. To observe the growth behavior of individual waves a Fourier decomposition is needed. This has been done for the u velocity at $y = 0$ at various downstream distances. The growth rates s computed are 0.065, 0.108, 0.12 for St=0.0086, 0.021, 0.028, respectively. The exponential growth of the low frequency wave at St=0.0086 is observed about $65 \leq x \leq 75$, which is sufficient downstream where the vortex roll-up can occur. Linear wave behavior is found in the region of $x \leq 36$ and $x \leq 25$ for St of 0.021 and 0.028, respectively. Low frequency expansion given by Monkewitz and Huerre [13] yields the growth rate $s(St)$ at λ_s of $\frac{1}{3}$ to be 0.578, 0.111, 0.122, in the same order as above.

The profile of u'_{rms} is illustrated in Figure 13. In the early development region kinks appear on both sides of the peak near the center. The kink on the slower side of fluid is very sharp. This phenomenon has been reported in both the experimental literature [2,4,15] and the theoretical literature [12]. Figure 13-(a) is for the unforced flow. The u'_{rms} profile first develops into double humps, then evolves into a single peak further downstream. Figure 13-(b) also shows the same type of kink in the initial development, but quite a different shape forms downstream. With excitation at the preferred frequency a deep valley appears in the center area. This is similar to the phenomenon Browand [15] found when the shear flow is excited at near the most preferred frequency. As flow proceeds further downstream the profile evolves to a single peak as in the previous case. As shown in Figure 13-(c), u'_{rms} under a lower frequency forcing, which is away from the most preferred upstream frequency, takes on a character similar to the unforced flow. No deep valley is seen in the middle of the flow evolution.

Forcing is introduced to the initial shear to see the more organized flow structure. The transverse velocity v is given an oscillation of $\epsilon g(y) \sin \omega t$, where g is a Gaussian distribution. For a subsonic mixing of two streams of M=0.6 and 0.3 ϵ is given to be 0.01, and the forcing is given at the most preferred frequency of St=0.021. The angular frequency ω is $\frac{2\pi}{11.785}$, which is 5.2 K Hz for the flow condition given. Figure 14 is the vorticity contours at consecutive time periods 192 μ seconds apart. As shown in Figures 6-9, vortices do not appear to be periodic in the unforced flow, the spacing between two consecutive vortices is irregular, and vortex roll-up and merging of two or even three vortices occurs randomly. However, in the presence of forcing, the initial vortex pairing process is suppressed, with the process resumed at some downstream location. Vortices are orderly, keeping the same distance apart. This is similar to the situation that Ho and Huang [14] observed. As shown in Figure 14, forcing generates a very organized flow structure. This figure also shows that the first five vortices appear frozen, in other words the flow up to about five vortices downstream is stationary. That is the precise counterpart of the flow visualization made in the laboratory using conditional sampling technique, which can be obtained by synchronizing the strobe speed with the forcing frequency. Vortex pairing occurs downstream, consequently, the flow appears to be unsteady in shedding vortices. This vorticity contour also gives the convective velocity to be 0.99, which is the same value found for the unexcited case.

A forced supersonic free shear flow is also computed with M=1.6 and 1.2. All of the velocity, temperature, and density are given at the inlet. All of the characteristic equations are imposed at the exit as the boundary conditions. Unlike subsonic flow, it is very difficult (at least in the present computation) to simulate the supersonic shear flow without excitation. This indicates that the nature of free shear flow generated by two supersonic streams is far more stable than the subsonic flow. External excitation of $\epsilon = 0.05$ is imposed on the v velocity at the inlet in a similar manner as used in subsonic flow. The forcing frequency ω is taken arbitrarily to be $\frac{2\pi}{12.29}$. Figure 15 shows the flow structure at every two time periods, which is at 128.9 μ seconds apart. The supersonic computation has been performed on Grid I. It is interesting to observe that no vortex pairing occurs. Many experiments have revealed that the free shear of two supersonic streams exhibits poor mixing characteristics, which is an indication of a very stable flow situation. All of the vorticity contour appears identical because conditional sampling is made on the flow field which is free of vortex paring processes. Again, the convective velocity computed from Figure 15 is 0.99. This value is in agreement with Papamoschou and Roshko [11]. From these observation of the excited shear flows it can be concluded that the forcing has no influence on the convective velocity.

Future Direction Towards Aeroacoustics

The fourth order numerical schemes developed in this work present flow solutions which exhibit important flow phenomena and agrees very well with published experiment and theory. As mentioned briefly in the introduction the flow field so simulated will be used as a source of the sound. There are two main ways to predict far-field noise from the numerical flow solution. The first approach is the acoustic analogy by Lighthill [1]. In this method, a numerical solution of the wave equation for a far-field is not required since the integral form of the exact solution is used, which is called the retarded potential solution. The computed flow solution is fed into the integrand and is to be integrated over the entire flow domain. Since the integrand is evaluated at different retarded times, a time interpolation is needed. Therefore, flow solutions must stored at several time steps over the entire flow regime.

A second way is to solve the wave equation directly, which can be done parallel to the flow field computation. A flow boundary is imposed sufficiently far from the center of the free shear layer, so that acoustic assumption is deemed plausible there. The wave equation is solved from a surface near the flow boundary with the pressure or density distribution given on it. The mesh in the wave equation computation is much larger than that used in the flow computation and becomes stretched greatly. The schematic is drawn in Figure 16. An accurate wave equation solver is an essential tool for this purpose. A higher order DRP scheme seems to be a good choice to solve the wave equation.

It is acknowledged that Dr S.T. Yu's work was a benefit to the present development of numerical methods.

References

1. M.J. Lighthill, On sound generated aerodynamically I. General theory, Proc. Roy. Soc. A, vol. 211, 564-587, 1952.

2. P. Freymuth, On transition in a separated laminar boundary layer, J. Fluid Mech. vol. 25, 683-704, 1966.

3. G.L. Brown and A. Roshko, On density effects and large structure in turbulent mixing layers, J. Fluid Mech. vol. 64, 775-816, 1974.

4. C.D. Winant and F.K. Browand, Vortex pairing mechanism of turbulent mixing-layer growth at moderate Reynolds number, J. Fluid Mech. vol. 63, 237-255, 1974.

5. S.K. Lele, Direct numerical simulation of compressible free shear flow, AIAA paper 89-0374, 1989.

6. S.T. Yu, Y.-L.P. Tsai and K.C. Hsieh, Runge-Kutta methods combined with compact difference schemes for the unsteady Euler equations, AIAA paper 92-3210, 1992.

7. C.K.W. Tam and J.C. Webb, Dispersion-Relation-Preserving finite difference schemes for computational acoustics, will appear in J. Comput. Phys.

8. A. Jameson, W. Schmidt and E. Turkel, Numerical solution of the Euler equations by finite volume methods using Runge-Kutta time stepping schemes, AIAA paper 81-1259, 1981.

9. G.W. Hedstrom, Nonreflecting boundary conditions for nonlinear hyperbolic systems, J. Comput. Phys. vol. 30, 222-237, 1979.

10. K.W. Thompson, Time dependent boundary conditions for hyperbolic systems, J. Comput. Phys. vol. 68, 1-24, 1987.

11. D. Papamoschou and A. Roshko, Observations of supersonic free shear layers, AIAA paper 86-0162, 1986.

12. A. Michalke, On spatially growing disturbances in an inviscid shear layer, J. Fluid Mech., vol. 23, 521-544, 1965.

13. P.A. Monkewitz and P. Huerre, Influence of the velocity ratio on the spatial instability of mixing layers, Phys. Fluids, vol. 25, 1137-1143, 1982.

14. C.-M. Ho and L.-S. Huang, Subharmonics and vortex merging in mixing layers, J. Fluid Mech. vol. 119, 443-473, 1982.

15. F.K. Browand, An experimental investigation of the instability of an incompressible, separated shear layer, J. Fluid Mech. vol. 26, 281-307, 1966.

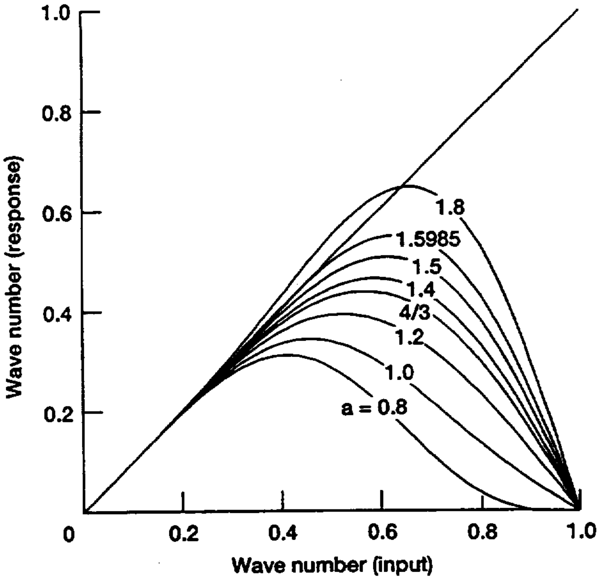

Figure 1.—Wave number relation in the explicit differencing scheme.

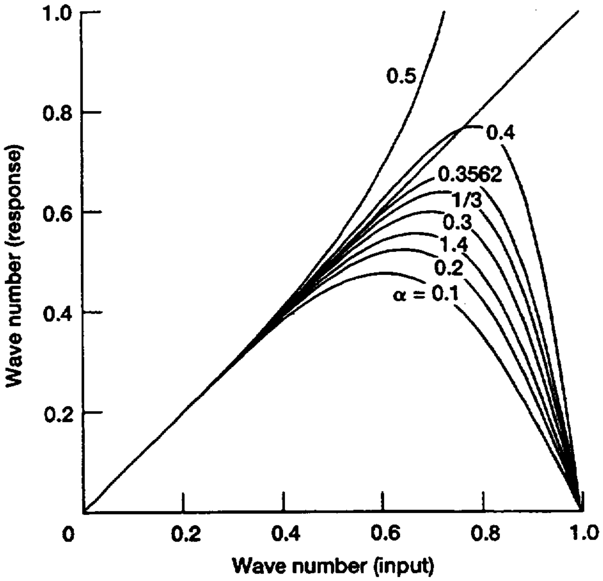

Figure 2.—Wave number relation in the implicit differencing scheme.

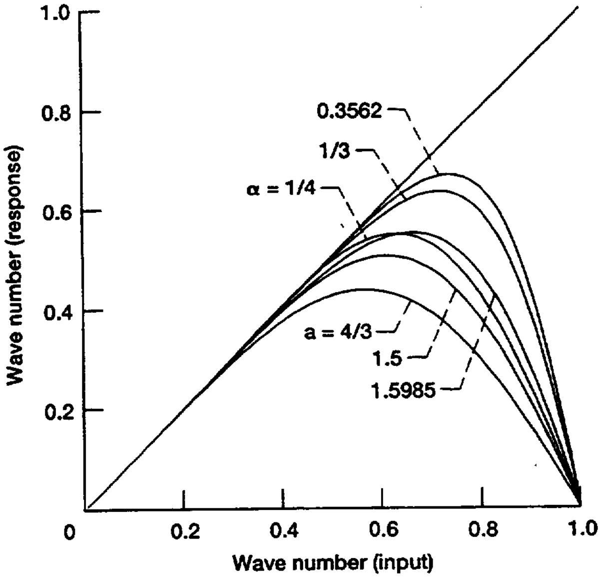

Figure 3.—Wave number relation in the explicit and implicit differencing scheme.

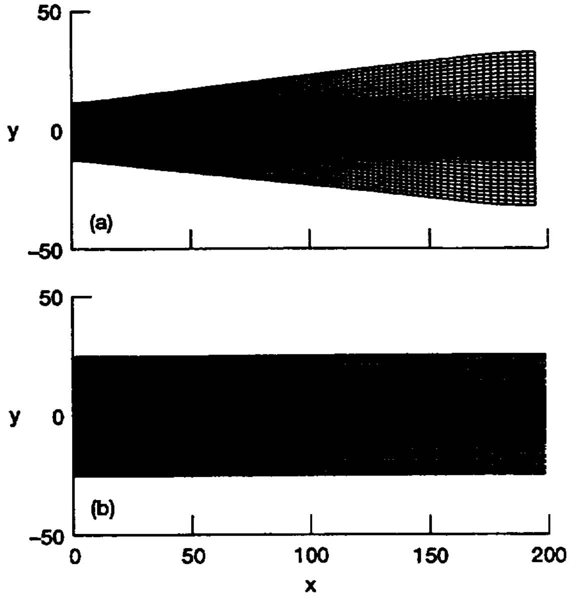

Figure 4.—(a) Grid I: 240x120 and (b) Grid II: 300x160.

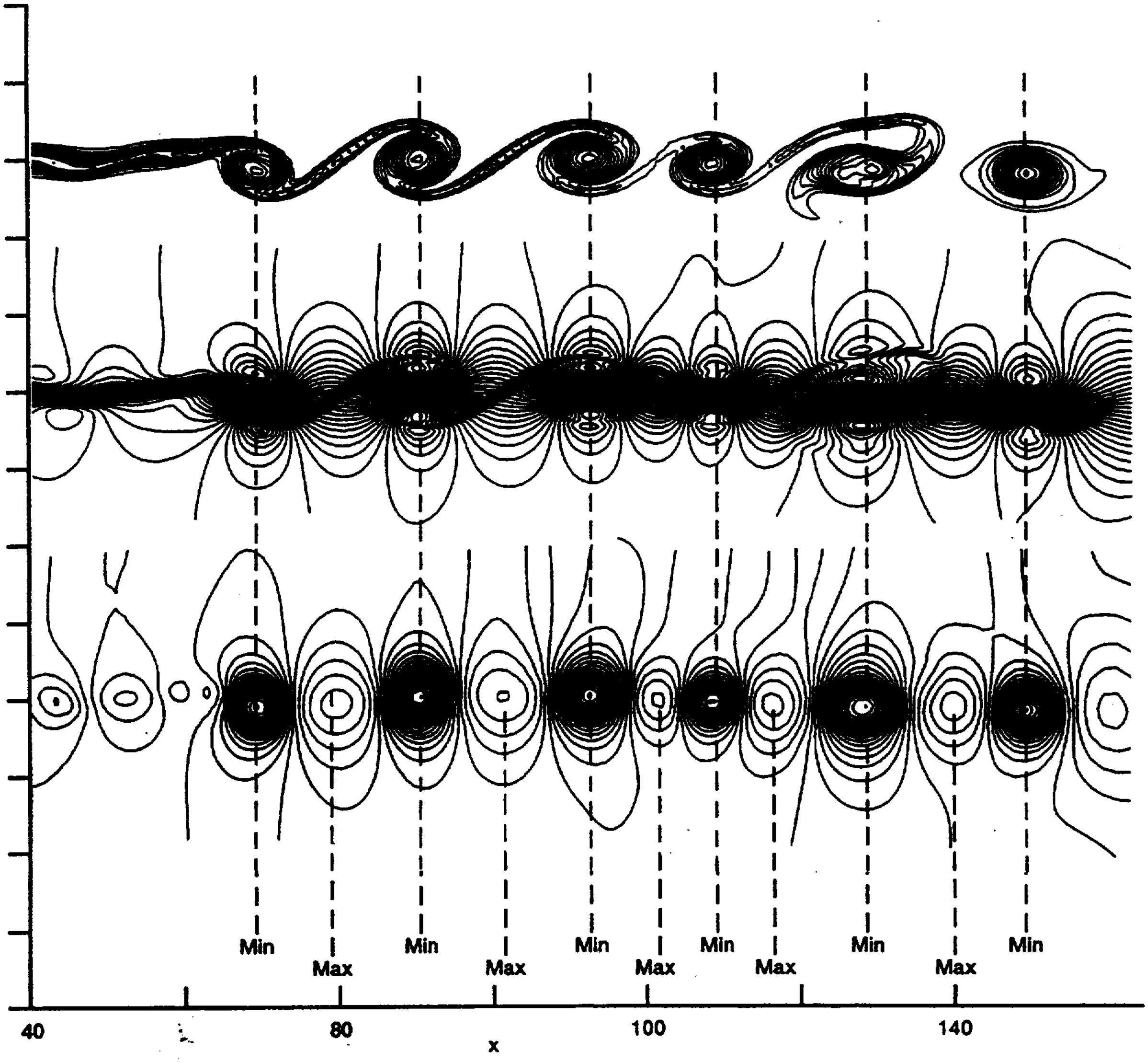

Figure 5.—Contours of (a) vorticity, (b) Mach number, and (c) static pressure.

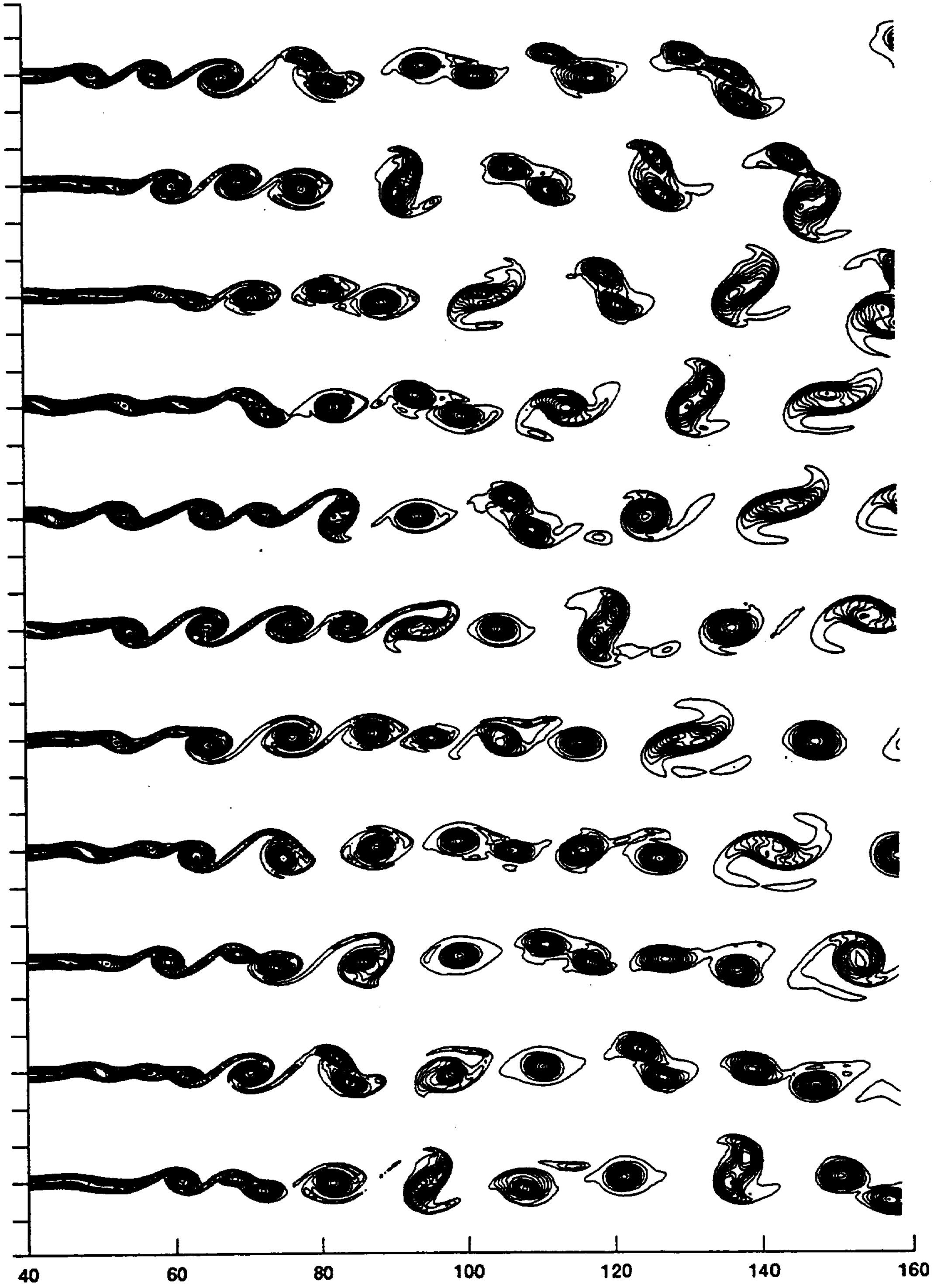

Figure 6.—Vorticity contour at every 200 Δt computed by Pade scheme with optimum α.

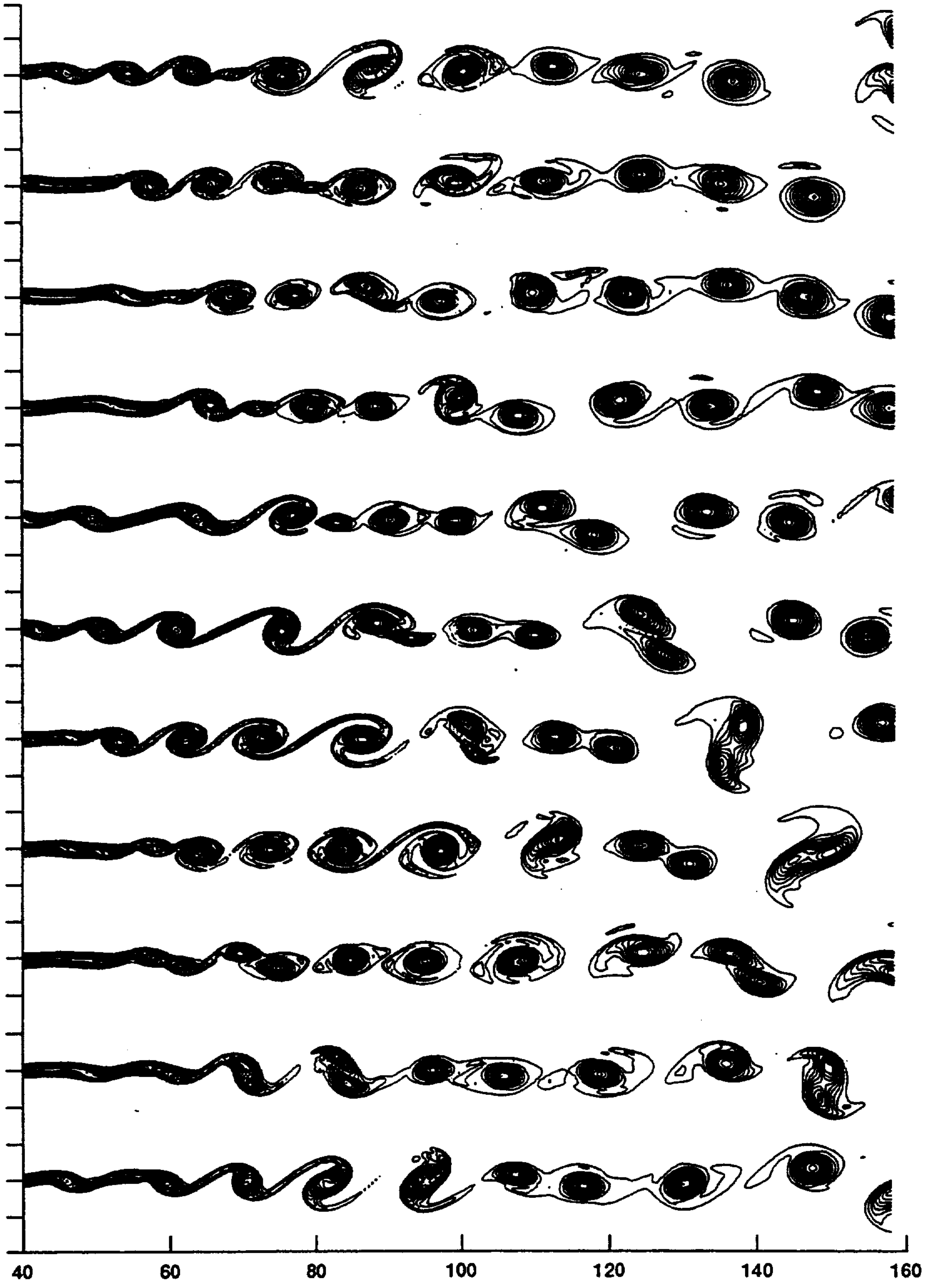

Figure 7.—Vorticity contour at every 200 Δt computed by Pade scheme with α = 0.3.

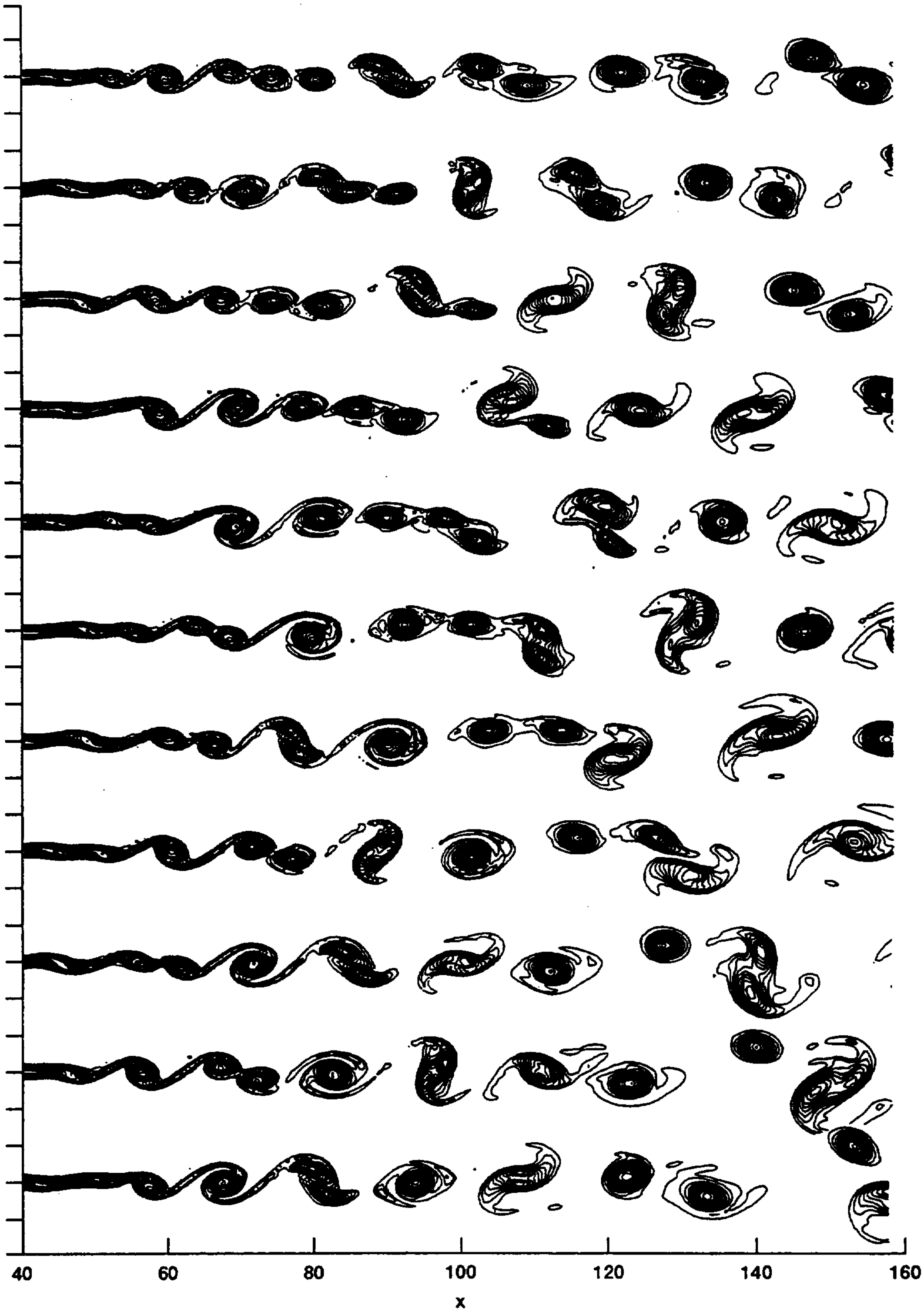

Figure 8.—Vorticity contour at every 200 Δt computed by DRP explicit scheme with a = 1.59853.

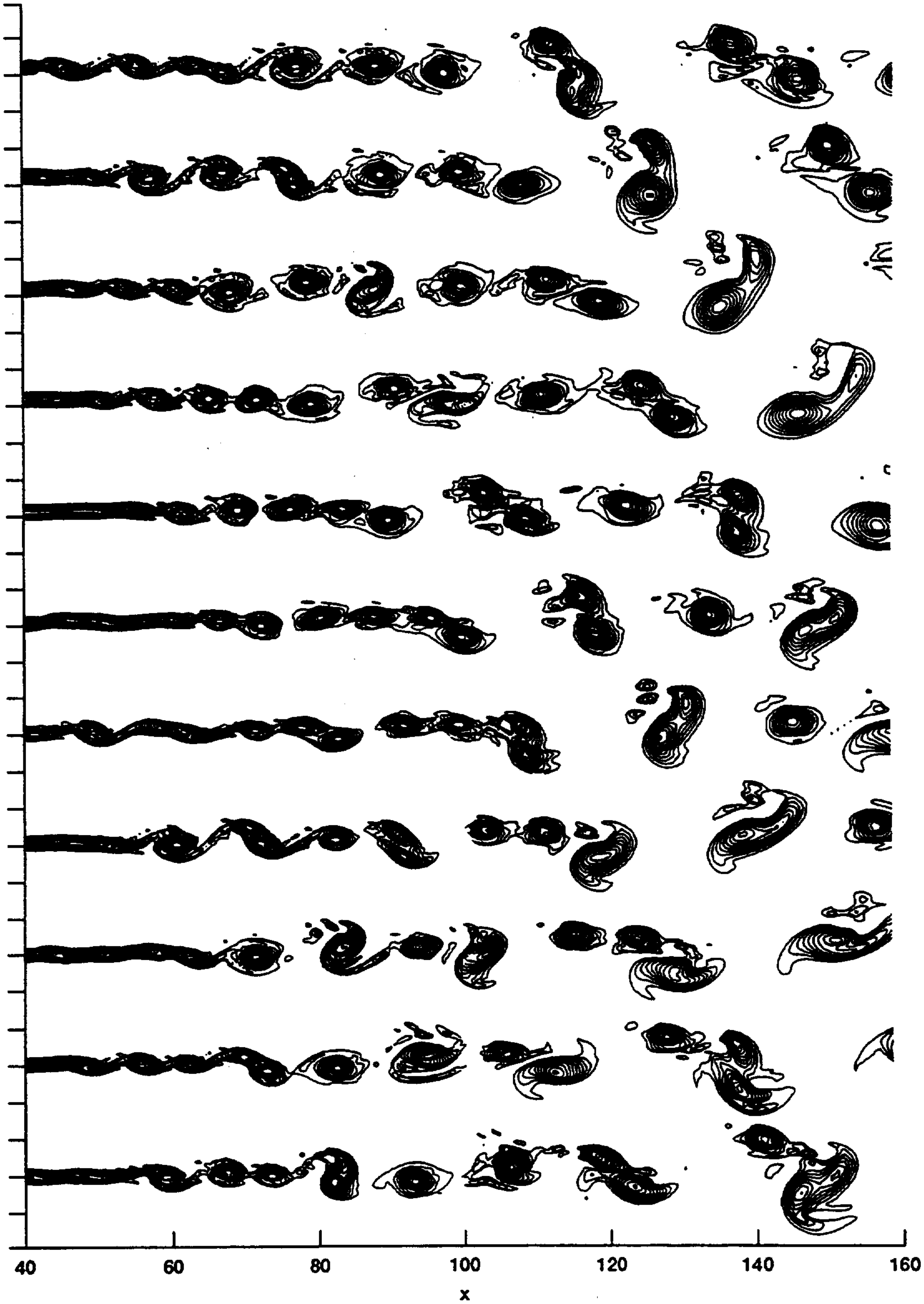

Figure 9.—Vorticity contour at every 200 Δt computed by explicit scheme with a = 4/3.

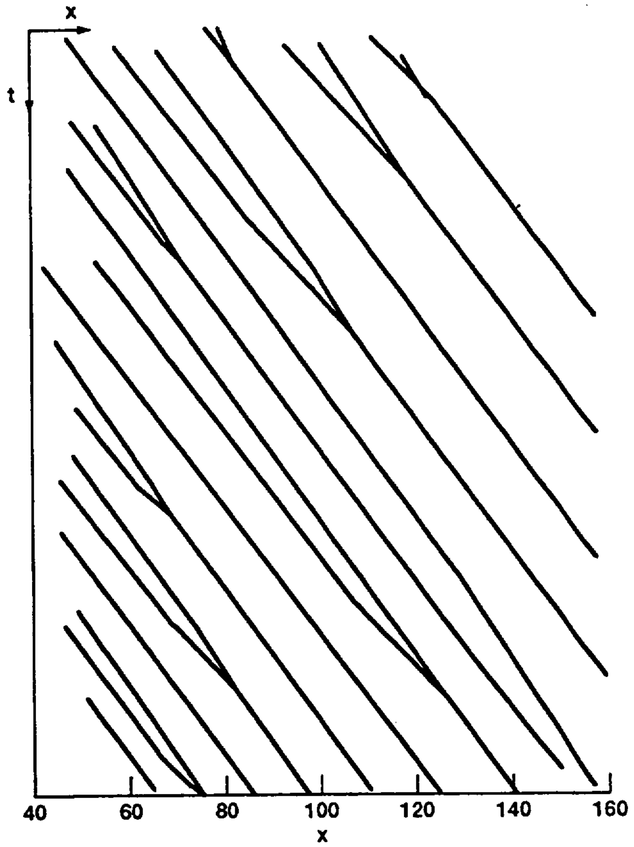

Figure 10.—Trajectory of vortices.

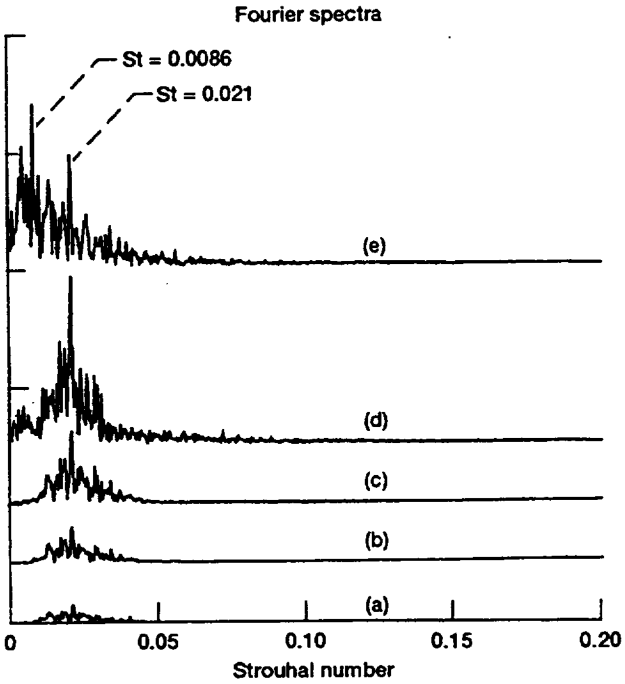

Figure 11.—Fourier spectra of the u velocity at y = 0; (a) x = 20.65, (b) x = 27.65, (c) x = 34.65, (d) x = 52.84 (e) x = 94.14.

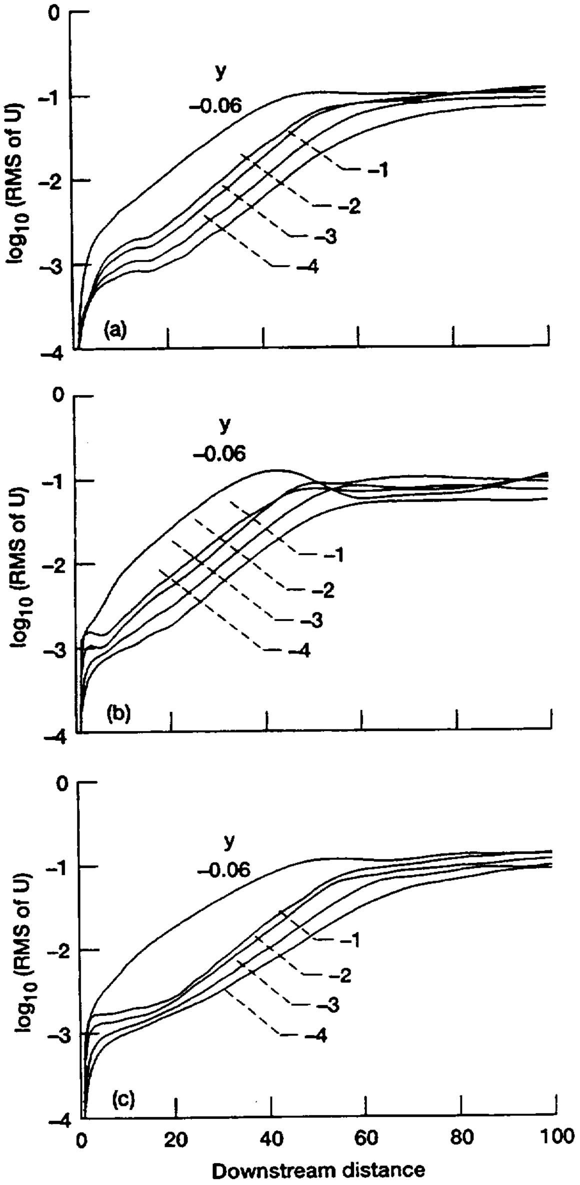

Figure 12.—The growth of turbulence intensity u_{rms} along x; (a) unforced, (b) forced with *St* = 0.021, (c) forced with *St* = 0.0086.

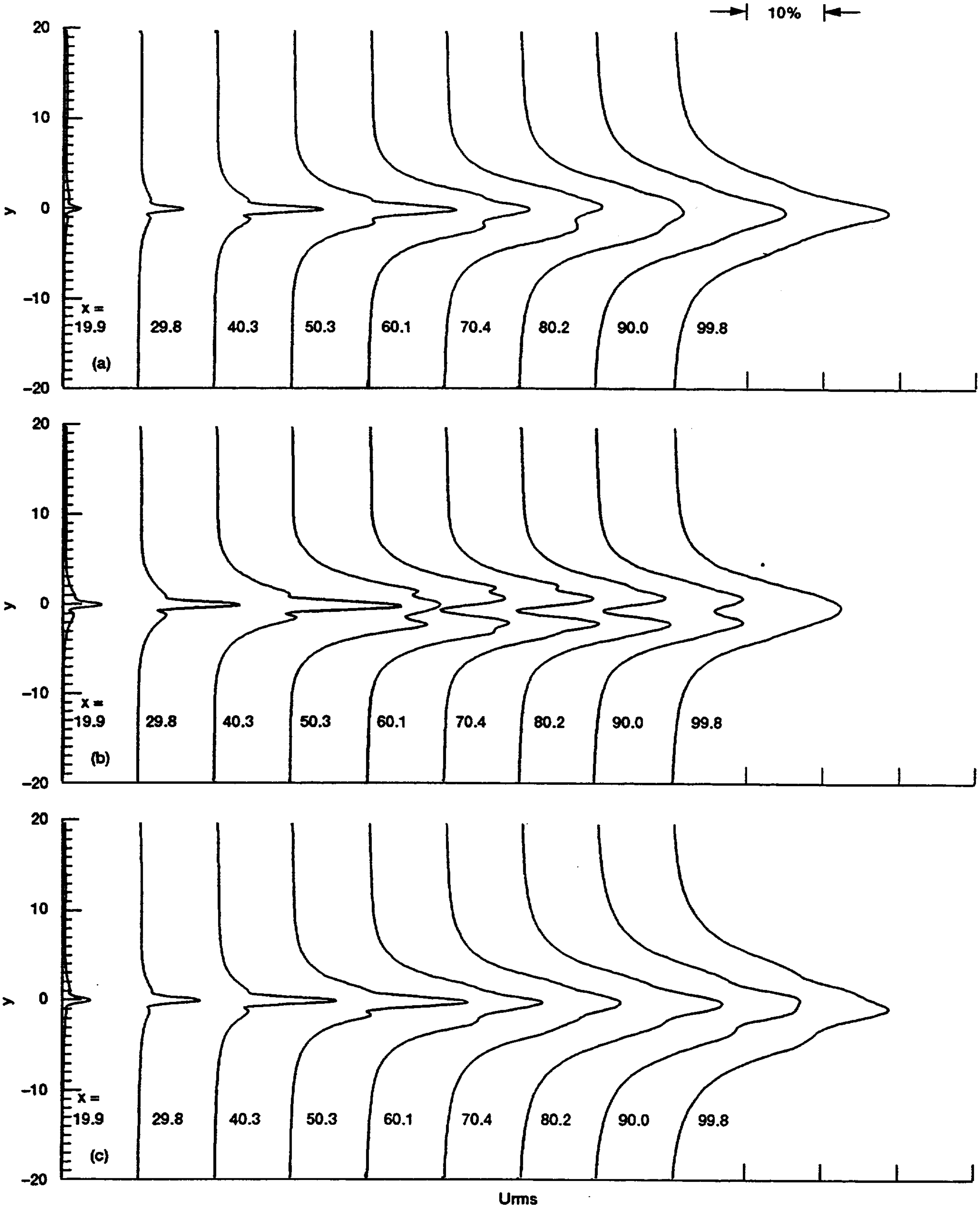

Figure 13.—u_{rms} profile; (a) unforced, (b) forced with St = 0.021, (c) forced with St = 0.0086.

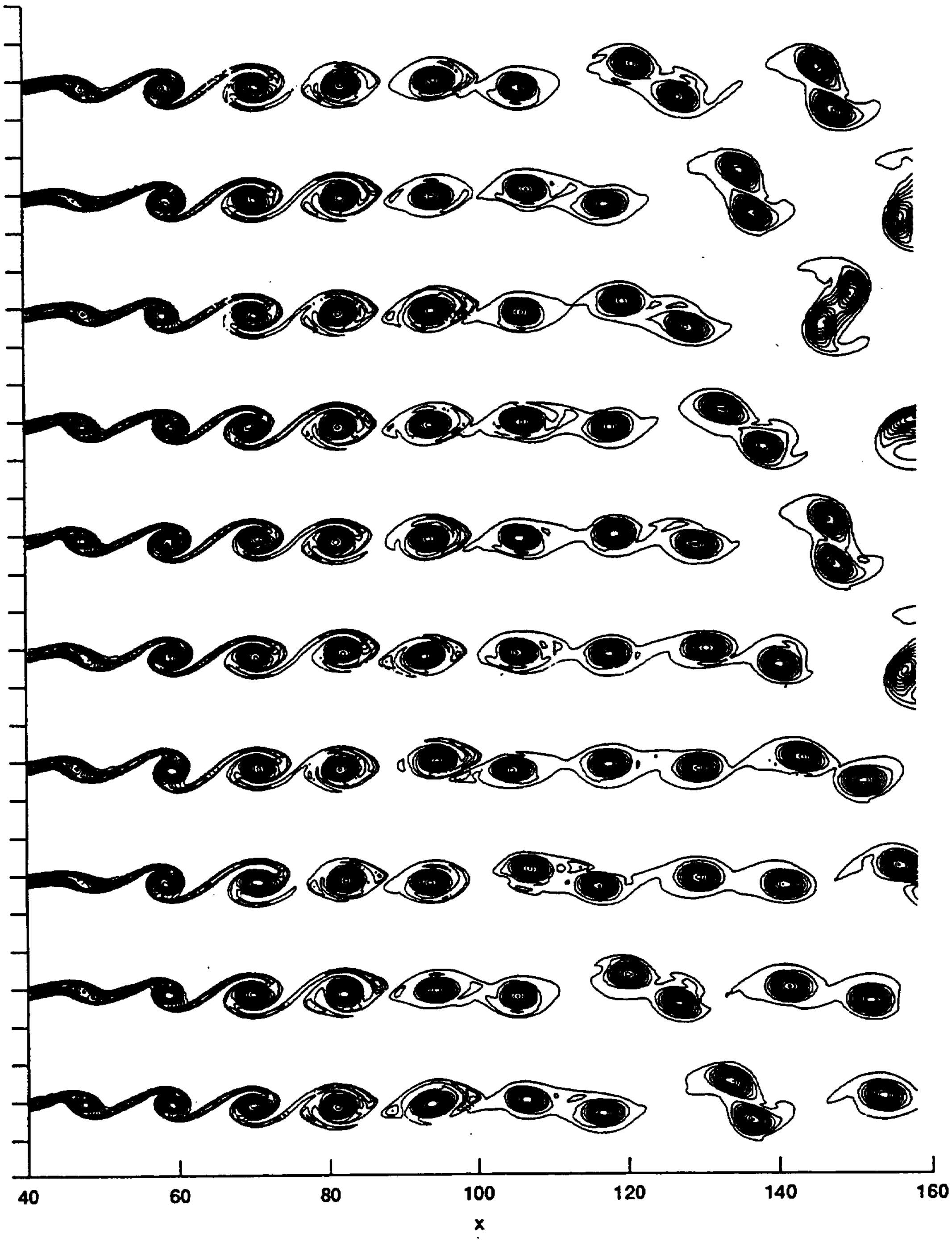

Figure 14.—Vorticity contours of forced subsonic flow at every period.

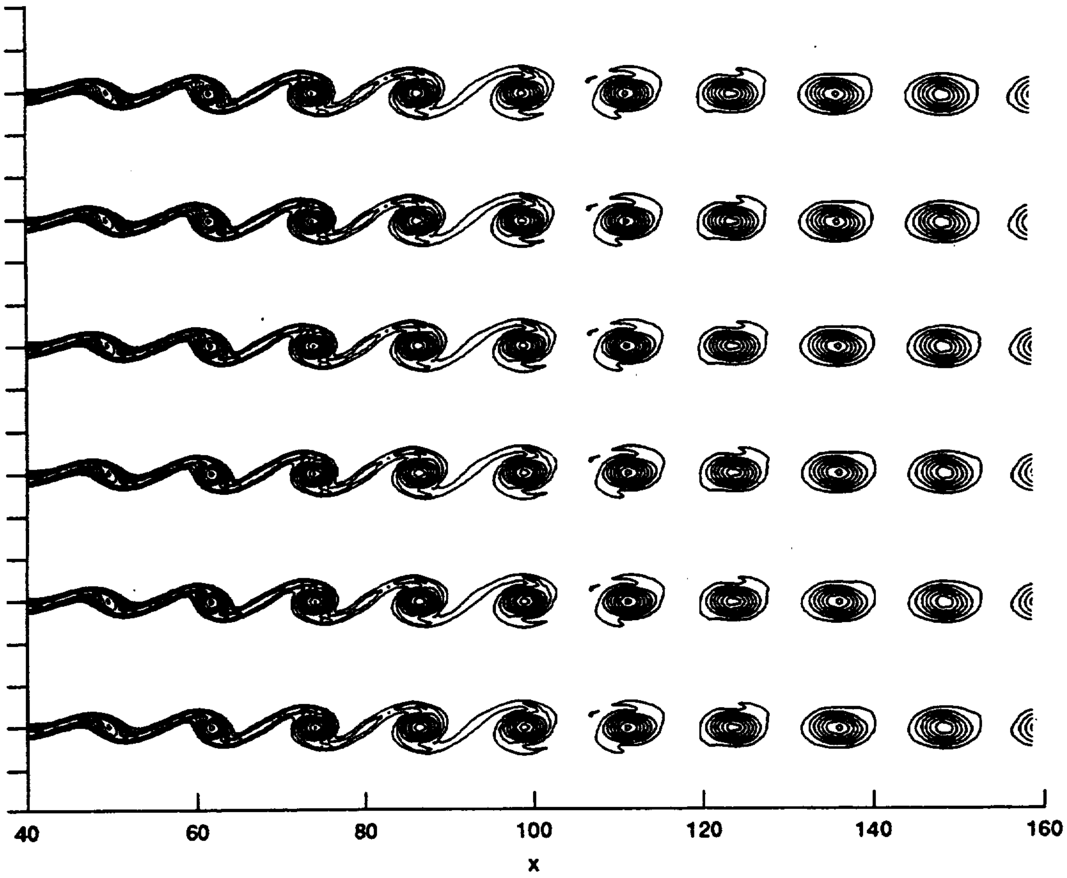

Figure 15.—Vorticity contours of forced supersonic flow at every two period.

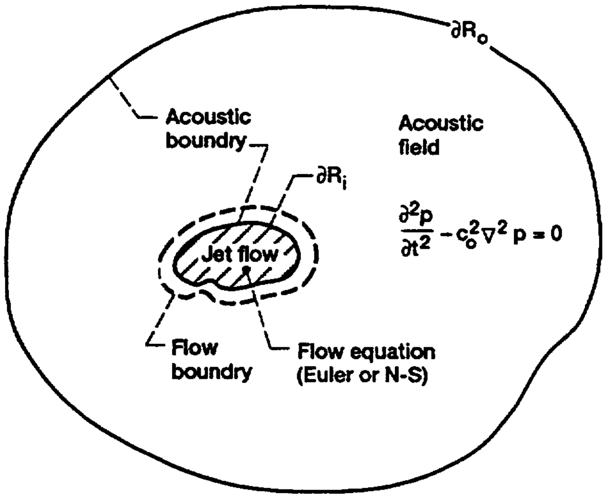

Figure 16.—Schematics of flow and wave computation regions.

REPORT DOCUMENTATION PAGE

Form Approved
OMB No. 0704-0188

1. AGENCY USE ONLY (*Leave blank*)

2. REPORT DATE
April 1993

3. REPORT TYPE AND DATES COVERED
Final Contractor Report

4. TITLE AND SUBTITLE
Numerical Simulation of Free Shear Flows-Towards a Predictive Computational Aeroacoustics Capability

5. FUNDING NUMBERS
WU-505-62-52
C-NAS3-25266

6. AUTHOR(S)
W.Y. Soh

7. PERFORMING ORGANIZATION NAME(S) AND ADDRESS(ES)
Sverdrup Technology, Inc.
Lewis Research Center Group
2001 Aerospace Parkway
Brook Park, Ohio 44142

8. PERFORMING ORGANIZATION REPORT NUMBER
E-7821

9. SPONSORING/MONITORING AGENCY NAME(S) AND ADDRESS(ES)
National Aeronautics and Space Administration
Lewis Research Center
Cleveland, Ohio 44135-3191

10. SPONSORING/MONITORING AGENCY REPORT NUMBER
NASA CR-191015

11. SUPPLEMENTARY NOTES
Project Manager, James R. Scott, Internal Fluid Mechanics Division, (216) 433-5863.

12a. DISTRIBUTION/AVAILABILITY STATEMENT
Unclassified - Unlimited
Subject Category 02

12b. DISTRIBUTION CODE

13. ABSTRACT ***(Maximum 200 words)***

Implicit and explicit spatial differencing techniques with fourth order accuracy have been developed. The implicit technique is based on the Pade compact scheme. A Dispersion Relation Preserving concept has been incorporated into both of the numerical schemes. Two dimensional Euler computation of a spatially-developing free shear flow, with and without external excitation, has been performed to demonstrate the capability of numerical schemes developed. Results are in good agreement with theory and experimental observation regarding the growth rate of fluctuating velocity, the convective velocity, and the vortex-pairing process.

14. SUBJECT TERMS
Shear flow; Large vortical structure; Vortex pairing; Pade compact scheme; DRP scheme

15. NUMBER OF PAGES
26

16. PRICE CODE
A03

17. SECURITY CLASSIFICATION OF REPORT
Unclassified

18. SECURITY CLASSIFICATION OF THIS PAGE
Unclassified

19. SECURITY CLASSIFICATION OF ABSTRACT
Unclassified

20. LIMITATION OF ABSTRACT

NSN 7540-01-280-5500

Standard Form 298 (Rev. 2-89)
Prescribed by ANSI Std. Z39-18
298-102